Volume 10
Number 12
December 2023
Pages 5317–5986

Materials Horizons

rsc.li/materials-horizons

ISSN 2051-6347

ROYAL SOCIETY OF CHEMISTRY

COMMUNICATION

Wei Tao, Tiangang Luan, Seyoung Koo, Xiaoyuan Ji *et al.*
Infected wound repair with an ultrasound-enhanced nanozyme hydrogel scaffold

Materials Horizons

ROYAL SOCIETY OF CHEMISTRY

COMMUNICATION

View Article Online
View Journal | View Issue

Cite this: *Mater. Horiz.*, 2023, **10**, 5474

Received 8th July 2023,
Accepted 29th August 2023

DOI: 10.1039/d3mh01054f

rsc.li/materials-horizons

Infected wound repair with an ultrasound-enhanced nanozyme hydrogel scaffold†

Fan Zhang, ‡[afg] Yong Kang,‡[b] Liwen Feng,[c] Guan Xi,[afg] Wei Chen,[e] Na Kong,[e] Wei Tao, *[e] Tiangang Luan,*[af] Seyoung Koo*[e] and Xiaoyuan Ji *[bd]

Chronic diabetic wounds persistently face the threat of evolving into diabetic foot ulcers owing to severe hypoxia, high levels of reactive oxygen species (ROS), and a complex inflammatory microenvironment. To concurrently surmount these obstacles, we developed an all-round therapeutic strategy based on nanozymes that simultaneously scavenge ROS, generate O_2 and regulate the immune system. First, we designed a dynamic covalent bond hybrid of a metal–organic coordination polymer as a synthesis template, obtaining high-density platinum nanoparticle assemblies (PNAs). This compact assembly of platinum nanoparticles not only effectively simulates antioxidant enzymes (CAT, POD) but also, under ultrasound (US), enhances electron polarization through the surface plasmon resonance effect, endowing it with the ability to induce GSH generation by effectively replicating the enzyme function of glutathione reductase (GR). PNAs, by mimicking the activity of CAT and POD, effectively catalyze hydrogen peroxide, alleviate hypoxia, and effectively generate GSH under ultrasound, further enhancing ROS scavenging. Notably, PNAs can regulate macrophage responses in the inflammatory microenvironment, circumventing the use of any additives. It was confirmed that PNAs can enhance cell proliferation and migration, promote neoangiogenesis *IN VITRO*, and accelerate the healing of infected diabetic wounds *IN VIVO*. We believe that an all-round therapeutic method based on PNA nanozymes could be a promising strategy for sustained diabetic wound healing.

New concepts

Nanozymes, with nanoscale structures exhibiting enzyme-like properties, have been successfully applied in various fields. To date, nanozymes mainly focus on mimicking antioxidant enzymes such as catalase, peroxidase, superoxide dismutase, *etc.* The limited range of substrates and the narrow scope of catalytic types are the major limitations to nanozymes. Herein, a new concept of glutathione reductase-mimicking nanozymes is reported and developed as an all-round therapeutic strategy for diabetic wound healing. High-density platinum nanoparticle assembly (PNA) nanozymes are prepared using a dynamic covalent bond hybrid of a metal–organic coordination polymer as a synthesis template. PNAs not only effectively simulate antioxidant enzymes but also endow them with the ability to induce GSH generation by effectively replicating glutathione reductase under ultrasound. Hence, an all-round therapeutic strategy based on nanozymes that simultaneously scavenge ROS, generate O_2 and regulate the immune system is achieved. It was confirmed that PNAs can enhance cell proliferation and migration, promote neoangiogenesis *in vitro*, and accelerate the healing of diabetic wounds *in vivo*. To the best of our knowledge, this is the first study to report glutathione reductase-mimicking nanozymes and provides a strong experimental basis for applying this strategy in other biomedical applications.

Introduction

Diabetic wounds, emerging as serious chronic wounds, are some of the most common complications faced by diabetic patients, thereby escalating the peril of limb amputation.[1] The pervasive incidence of chronic diabetic wounds among the staggering global populace of nearly 537 million individuals afflicted with diabetes is a global health problem.[2] The recuperative trajectory aimed at reinstating skin integrity and equilibrium postinjury represents a complex, dynamically evolving process, including various stages, such as hemostasis, inflammation, and cellular proliferation.[3,4] Nevertheless, glycated

[a] *School of Biomedical and Pharmaceutical Sciences, Guangdong University of Technology, Guangzhou 510630, P. R. China*
[b] *Academy of Medical Engineering and Translational Medicine, Medical College, Tianjin University, Tianjin, 300072, China. E-mail: jixiaoyuan@tju.edu.cn*
[c] *Boji Pharmaceutical Research Center, Boji Medical Biotechnological Co. Ltd, Guangzhou 510630, P. R. China*
[d] *Medical College, Linyi University, Linyi 276000, China*
[e] *Center for Nanomedicine and Department of Anesthesiology, Brigham and Women's Hospital, Harvard Medical School, Boston, MA, 02115, USA. E-mail: wtao@bwh.harvard.edu, hs8019@uhs.ac.kr*
[f] *Jieyang Branch of Chemistry and Chemical Engineering Guangdong Laboratory (Rongjiang Laboratory), Jieyang 515200, China. E-mail: cesltg@gdut.edu.cn*
[g] *Smart Medical Innovation Technology Center, Guangdong University of Technology, Guangzhou 510630, P. R. China*
† Electronic supplementary information (ESI) available. See DOI: https://doi.org/10.1039/d3mh01054f
‡ F. Z and Y. K. contributed equally to this work.

residues are present in diabetic wounds. Hyperglycemia not only hampers the polarization of proinflammatory M1 macrophages into their anti-inflammatory M2 macrophages, thereby causing excessive accumulation of M1 macrophages but also increases the levels of advanced glycation end-products (AGEs).[5,6] Furthermore, it prompts the overexpression of reactive oxygen species (ROS), thus inducing hyperactivation of inflammatory cells and matrix metalloproteinases (MMPs).[7–9] The above features contribute to a microenvironment characterized by enduring inflammation and oxidative stress at the wound site, disrupting intracellular equilibrium and prompting the excessive production of inflammatory factors, thereby impeding the wound-healing process. Consequently, controlling local inflammation in diabetic wounds emerges as a pivotal step in the treatment of diabetic wound healing.[10–12]

Nanozymes, representing a category of substances that adeptly emulate natural cascade catalytic systems within complex physiological environments, exhibit several advantages, including low cost, efficient catalysis, and robust modifiability.[13–16] These qualities of nanozymes enable them to effectively overcome the inherent drawbacks of natural enzymes, such as poor stability and strong environmental dependencies. A series of nanozymes with iron, copper, gold, platinum, cerium, and carbon dots have been demonstrated to mimic some natural antioxidants (such as SOD, POD, CAT, GPx, *etc.*) or intrinsic antioxidant catalytic cascade systems.[17–19] Given their excellent stabilities and ROS scavenging capabilities, these nanozymes have been acclaimed as efficacious anti-inflammatory tools.[20,21] Nevertheless, solely reducing the inflammatory factor expression of the inflammatory microenvironment often proves insufficient to address the root conundrum of an imbalance within the homeostasis of inflammatory cells. As a result, the necessity for contriving anti-inflammatory mechanisms that accomplish synchronous ROS elimination and cellular homeostasis adjustment becomes apparent.[22,23]

Glutathione (GSH), an endogenous antioxidant, functions as the body's natural reducing agent and is predominantly synthesized *via* the action of glutathione reductase under the catalytic influence of the coenzyme NADPH. Beyond its role in orchestrating the regulation of intracellular redox equilibrium, it assumes a critical biological function in upholding intracellular homeostasis.[24–26] Platinum, a desired heterogeneous hydrogenation catalyst, facilitates the transfer of hydrogen atoms to the π orbitals of carbon through surface activation, thereby effectuating hydrogenation reactions.[27,28] Additionally, platinum, a soft acid, displays a robust affinity and rapid reaction rate with sulfur-containing soft base groups.[29] This characteristic bears semblance to the glutathione reductase-mediated process of regulating the GSSG/GSH ratio, utilizing NADPH as a coenzyme. While nanozymes composed of platinum nanoparticles or platinum nanoparticle assemblies have been confirmed to present antioxidant enzymatic activities, such as CAT and POD, which aid in ROS scavenging, it remains to be verified whether they can mimic the catalytic activity of glutathione reductase and regulate endogenous GSH.

Herein, we developed a synthesis approach for the self-assembly of platinum nanoparticles, drawing on the strategic utilization of a dynamically covalent bond, hybridized metal–organic coordination polymer as a template. This synthetic strategy modifies the distance between platinum nanoparticles *via* nanoconfinement, yielding dense platinum-based nanoparticle assemblies (PNAs). A series of enzyme kinetics studies have verified that PNAs not only maintain CAT or POD enzyme-like activities but also mimic the catalytic capability of glutathione reductase (GR) due to surface plasmon resonance effects with these dense Pt nanoparticles under ultrasonic mediation,[30] regulating GSH generation with the help of the coenzyme NADPH. The platinum-based nanosphere assemblies were mixed with GelMA hydrogel and applied in the diabetic wound model. By relieving hypoxia, scavenging ROS, and generating GSH, PNAs can restore the proliferation ability of fibroblasts and endothelial cells, enhance the migration of keratinocytes, and promote macrophage polarization to M2-type macrophages, leading to anti-inflammatory effects and accelerated healing of infected wounds (Fig. 1).

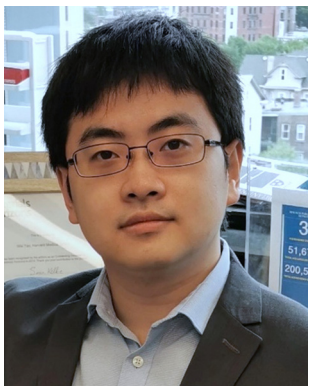

Wei Tao

Over the past decade, Materials Horizons has become an invaluable platform for groundbreaking discoveries, transformative ideas, and collaborative efforts amongst the brightest minds worldwide. Your pursuit of excellence has undoubtedly pushed the boundaries of knowledge, revolutionizing the way we understand and harness the potential of materials in all their forms. I am a regular reader of papers published in Materials Horizons, as well as one of the active reviewers for your journal. We look forward to future opportunities to publish our best work in Material Horizons. Congratulations on this significant milestone!.

Results and discussion

PNA preparation and characterization

PNAs were synthesized *via* a hydrothermal synthesis approach under acid catalysis, employing an imine-triazinebenylpyridine ligand and Pt(II). The imine-triazinebenylpyridine ligand was prepared by condensation of 4-pyridinecarbaldehyde and 2,4,6-tris(4-aminophenyl)-1,3,5-triazine in the presence of a catalytic amount of trifluoroacetic acid. The features and purity of the imine-triazinebenylpyridine ligand were confirmed by ^{1}H nuclear magnetic resonance (Fig. S1, ESI†). Studies carried out using transmission electron microscopy (TEM) confirmed the well-defined spherical morphologies of the synthesized PNAs, which were uniform in size. Additionally, high-magnification TEM images revealed the encapsulation of platinum nanoparticles (Pt NPs) ranging between 2 and 10 nm within the outer supporting structure, providing further insights into the structure of these individual PNAs (Fig. 2a).

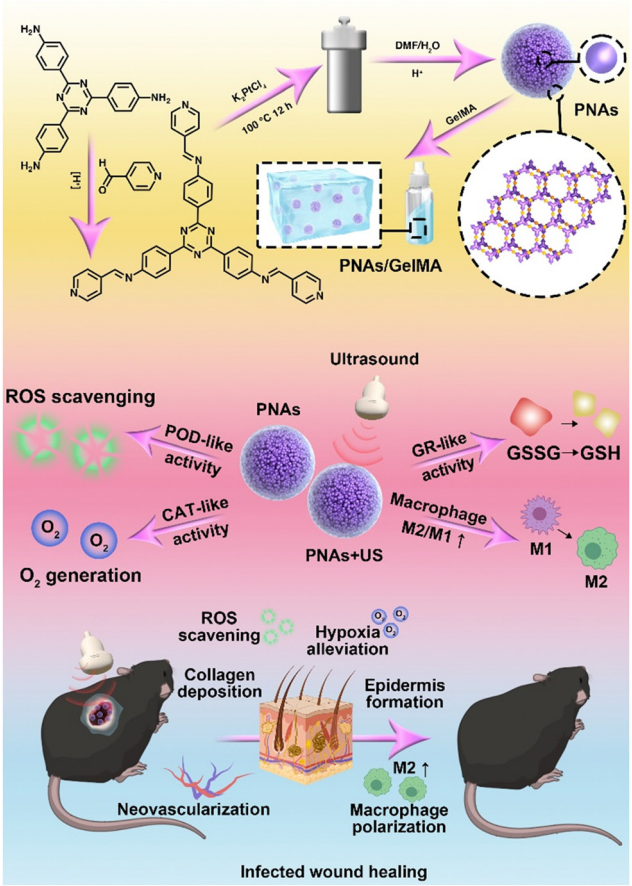

Fig. 1 Schematic illustration of the preparation and mechanism of GelMA + PNAs under the ultrasound wound healing strategy.

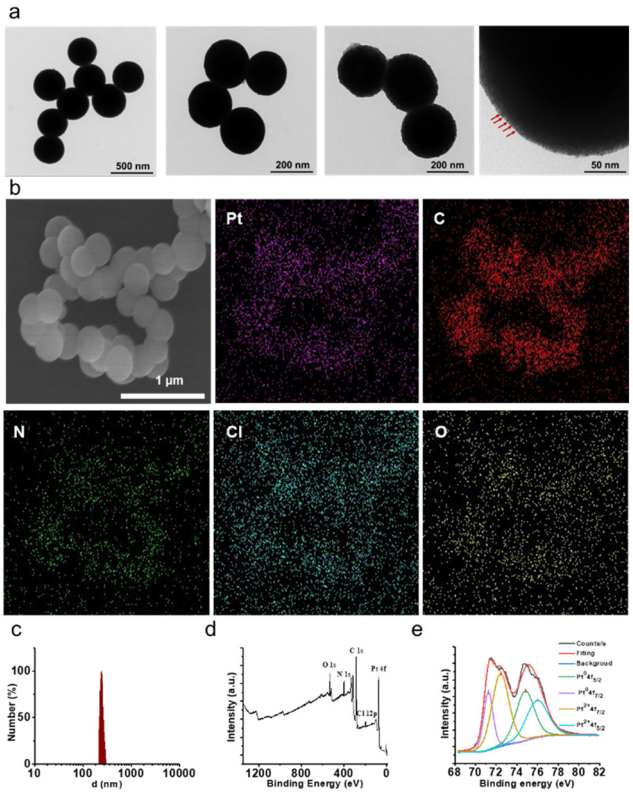

Fig. 2 Characterization of PNAs. (a) Representative TEM images of prepared PNAs. (b) Representative SEM and elemental mapping images of prepared PNAs. (c) DLS pattern of PNAs. (d) and (e) XPS spectra of PNAs (Pt^{2+}: 4f7/2 brown; Pt^{2+}: 4f5/2 blue; Pt (0): 4f7/2 purple; Pt (0): 4f5/2 green).

Scanning electron microscopy-energy dispersive spectroscopy (SEM-EDS) analysis further validated the morphology and elemental composition of the PNAs. As depicted in Fig. 2b, the PNAs are evidently composed of uniform nanospheres, and the Pt, C, N, Cl, and O elements were distributed on the nanosphere surface, confirming the composition of the PNAs. Consistent with the observations from TEM and SEM analyses, dynamic light scattering experiments reveal that the PNAs exhibit an average particle diameter of 221 nm and a zeta potential value of −18.5 mV (Fig. 2c and Fig. S2, ESI†). X-ray photoelectron spectroscopy (XPS) analysis of the PNAs exhibited prominent peaks for O, N, C, Pt, and Cl (Fig. 2d). Peaks emerging at 71.23 eV (4f7/2) and 74.83 eV (4f5/2), alongside those at 72.43 eV (4f7/2) and 76.03 eV (4f5/2), confirmed the existence of dual chemical environments, Pt(0) and Pt^{2+}, respectively (Fig. 2e). Such a phenomenon further validated the successful formation of the PNAs. In addition, the 44 wt% platinum content within the PNAs was determined *via* inductively coupled plasma atomic emission spectroscopy (ICP-AES).

PNA enzyme-mimicking activity

To evaluate the capability of PNAs to mimic a variety of natural enzymes, we opted for substrates that are typically used by these natural enzymes under physiological conditions.[31–33] Catalase (CAT), an antioxidant enzyme ubiquitous in living organisms, can catalyze the decomposition of two molecules of H_2O_2 into two H_2O molecules and one O_2 molecule, shielding cells from the deleterious effects of H_2O_2. This makes CAT a crucial component in the biological antioxidant defense system. As shown in Fig. 3a and b, the concentration of dissolved oxygen produced by PNAs, as measured by a portable dissolved oxygen meter, increased correspondingly with the concentration of the H_2O_2 substrate. The velocity at which PNAs instigate the decomposition of H_2O_2 to produce O_2 correspondingly surges, displaying a robust linear correlation. This observation confirmed the adept competence of PNAs to catalyze H_2O_2. To elucidate the catalytic efficiency of PNAs underlying the catalase-mimetic enzymatic catalysis, a steady-state kinetic measurement was performed by varying the concentration of the H_2O_2 substrate (1–6 mM) at a fixed concentration of PNAs (2 μg mL^{-1}), following the Michaelis–Menten equation. Fitting analysis of the enzymatic kinetics curves revealed that the values of K_m and V_{max} for PNAs were 5.48 mM and 0.087 mg L^{-1} S^{-1}, respectively (Fig. 3c and d).

Regarded as another antioxidant enzyme, peroxidase (POD) is a biological enzyme that detoxifies H_2O_2 into H_2O. Typically, 3,3′,5,5′-tetramethylbenzidine (TMB) is employed as a chromogenic substrate for evaluating POD enzyme activity. In the

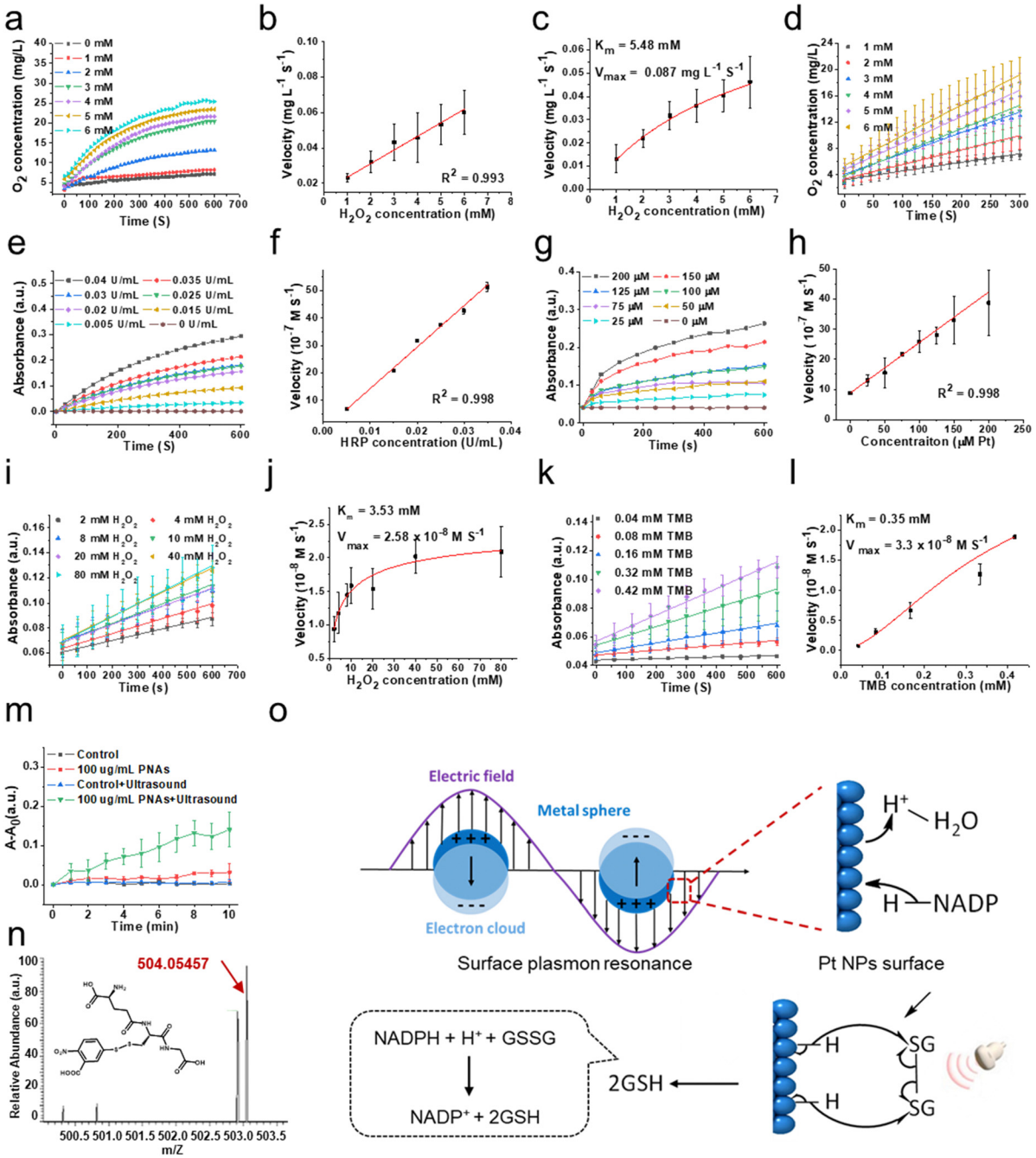

Fig. 3 The enzyme-like activity of PNAs. Catalase (CAT)-like activity of PNAs: (a) O_2 generation in the presence of PNAs (4.5 μM Pt) at various H_2O_2 concentrations. (b) The relationship between the initial reaction rate and H_2O_2 concentration in the presence of PNAs (4.5 μM Pt) at 300 seconds. (c) Initial O_2 concentration changes with time at different concentrations of PNAs (4.5 μM Pt) in deoxygenized H_2O at 25 °C. (d) Michaelis–Menten curve of the CAT-like activity of PNAs (n = 3 for each group). Peroxidase (POD)-like activity of PNAs: (e) the absorbance changes in the presence of TMB (0.2 mg mL^{-1}) at various HRP concentrations. (f) The relationship between the initial reaction rate and HRP concentration in the presence of TMB (0.2 mg mL^{-1}) at 600 seconds. (g) The absorbance changes in the presence of TMB (0.2 mg mL^{-1}) at various PNA concentrations. (h) The relationship between the initial reaction rate and PNA concentration in the presence of TMB (0.2 mg mL^{-1}) at 600 seconds. (i) Initial absorbance changes with time at different concentrations of H_2O_2 in the presence of PNAs (25 μM Pt) and TMB (0.2 mg mL^{-1}) in HAc-NaAc buffer at pH 5.8 and 25 °C. (j) Michaelis–Menten curve of the POD-like activity of PNAs using H_2O_2 as substrate. (k) Initial absorbance changes with time at different concentrations of TMB in the presence of PNAs (25 μM Pt), H_2O_2 (0.1 M) in HAc–NaAc buffer at pH 5.8 and 25 °C. (l) Michaelis–Menten curve of the POD-like activity of PNAs using TMB as substrate (n = 3 for each group). The GR-like activity of PNAs: (m) time-dependent absorbance changes in the presence of PNAs (100 μg mL^{-1}), GSSG (500 μM), DTNB (3 mg mL^{-1}), and NADPH (0.5 mg mL^{-1}) with and without ultrasound (1 MHz, 0.5 W cm^{-2}). (n = 3 for each group). (n) ESI-MS spectra (negative mode) of GS-TNB. (o) Schematic illustration of the GR-like activity of PNAs.

presence of TMB, the POD enzyme, while catalyzing the generation of H_2O from H_2O_2, transforms colorless TMB to blue oxidized TMB, which exhibits maximal characteristic absorption at 652 nm. Utilizing H_2O_2 as the substrate and TMB as the chromogenic agent, we compared the activity of natural POD enzyme and horseradish peroxidase (HRP) at different concentrations (Fig. 3e) with the POD-like activity of PNAs at varying concentrations of PNAs (Fig. 3g). The enzyme activity of PNAs at a Pt concentration of 200 μM (approximately 88 μg mL^{-1}) is commensurate with 0.04 U mL^{-1} HRP. Additionally, the reaction velocities of both escalate in parallel with an increase in substrate concentration, exhibiting a robust linear relationship (Fig. 3f and h). Subsequently, according to the Michaelis–Menten equation, we investigated the enzymatic catalytic activity of PNAs using H_2O_2 and TMB as substrates. The catalytic reaction rates of PNAs were enhanced by increasing the substrate concentration of either H_2O_2 or TMB (Fig. 3i and k). The kinetic curve fitting results for both substrates demonstrated K_m values of 3.53 mM (H_2O_2 as substrate) and 0.35 mM (TMB as substrate), with corresponding V_{max} values of 2.58×10^{-8} M S^{-1} and 3.3×10^{-8} M S^{-1}, respectively (Fig. 3j and l).

Glutathione reductase (GR) is one of the key enzymes in the intracellular glutathione redox cycle, playing a multifaceted biological role encompassing oxidative stress regulation, cellular signaling and transcription, detoxification, cellular function, and metabolism regulation. Employing reduced coenzyme II (NADPH), GR catalyzes the transformation of oxidized glutathione (GS-SG) into its reduced state (GSH), thereby executing its biological role. Following polarization on the surface of platinum nanoparticles, H atoms can transfer to the π orbitals of corresponding molecules, realizing the hydrogenation reaction. PNAs, as dense platinum nanoparticle assemblies, can further promote electron polarization and accelerate the hydrogenation process by the surface plasmon resonance effect under the influence of physical forces (Fig. 3o). In details, according to Mie's theory,[34] when light irradiates the surface of nanoparticles, substantially smaller than its wavelength, at a distinct frequency, the free electrons within the nanoparticles undergo resonance driven by the incident electromagnetic field. This plasmonic resonance effect allows the formation of a localized near-field electromagnetic enhancement field on and adjacent to the nanoparticle surface, further promoting the electron polarization, resulting to realizing the catalytic reaction.[35] PNAs have been determined to be a high-density platinum (0) nanoparticle assemblies. The cavitation effect induced by ultrasonic waves translates to light of a particular frequency that resonates with the PNAs, same as the photoexcitation. The electronic polarization of the Pt NPs surface caused by this surface plasmon resonance effect can accept the energy of a lone pair of electrons from NADPH, leading to form two separate electrons and activated H on the Pt NPs surface. Subsequently, the sustained ultrasonic influence radicalizes the disulfide bond of GS-SG, which then reacts with the activated H on the Pt NPs surface, resulting in the production of 2GSH.[36–38]

Therefore, we examined the capability of the PNAs to catalyze the production of GSH from GSSG, utilizing NADPH as a coenzyme under ultrasound (US) intervention. The interaction of 5,5′-dithiobis-(2-nitrobenzoic acid) (DTNB) with the thiol group of GSH yields the colored product GS-TNB, providing a reliable methodology for measuring GSH in solution. By employing UV spectrophotometry to scrutinize the temporal evolution of the GS-TNB characteristic absorption at 412 nm, we observed that the absorption variance of 100 mg mL^{-1} PNAs exposed to ultrasound (1 MHz, 0.5 W cm^{-2}) notably exceeded that of the control, ultrasound alone, and PNA only groups (Fig. 3m). This alludes to the proficient catalytic performance of PNAs in promoting GSH generation under ultrasound mediation. To further identify the formation of GS-TNB, high-resolution mass spectrometry was applied for product analysis. The characteristic peak for GS-TNB, observed at 503.05508 (negative ion mode) in the positive control group (pure GSH + DTNB), closely matched the theoretical value of 504.06 (Fig. S3 and S4, ESI†). An obvious peak at 503.05435 (negative ion mode) confirmed the presence of GS-DTNB in the PNAs + ultrasound group (Fig. 3n). Conversely, no distinctive peaks indicative of GS-TNB were observed in the control group (no PNAs) or the ultrasound alone group (no PNAs), affirming the capacity of PNAs to mimic GR in catalyzing the conversion of GSSG to GSH under ultrasound (Fig. S5 and S6, ESI†). Based on the results mentioned above, PNAs serve as a multifaceted nanozyme capable of effectively emulating the CAT and POD antioxidant enzymes, as well as the GR enzyme under ultrasound mediation.

ROS scavenging of PNAs *in vitro*

Wound healing is a collaborative process involving various cellular activities, such as fibroblast proliferation, keratinocyte migration, and endothelial cell differentiation. Hence, we first examined the biocompatibility of PNAs on fibroblasts (L929) and human umbilical vein endothelial cells (HUVECs). PNAs varying from 0–25 μg mL^{-1} demonstrated excellent cytocompatibility with both L929 and HUVECs (Fig. 4a). Diabetic wound features refer to the aggravation of ROS levels and persistent oxidative stress. Nanozymes, possessing antioxidant capabilities, have been proven to mitigate oxidative cell damage, thereby accelerating the healing of chronic wounds. An oxidative stress cell model stimulated by H_2O_2 was established to measure the ROS clearance rate and cell proliferation rate, thereby determining the antioxidant performance of PNAs. We further examined the effect of various concentrations of PNAs and PNAs under ultrasound radiation on the proliferation of L929 and HUVECs. Fig. 4b reveals that the proliferation rate of L929 and HUVECs induced by 5 mg mL^{-1} or 10 mg mL^{-1} PNAs was significantly higher than that of the H_2O_2 group, and there was no significant difference between the two concentration groups. Notably, the proliferation rates induced by PNAs + US were higher, with the rate in the 10 mg mL^{-1} PNAs + US group surpassing that in the 5 mg mL^{-1} PNAs + US group. This suggests that under US, the higher the PNA concentration is, the stronger the capacity to produce GSH and H_2O_2

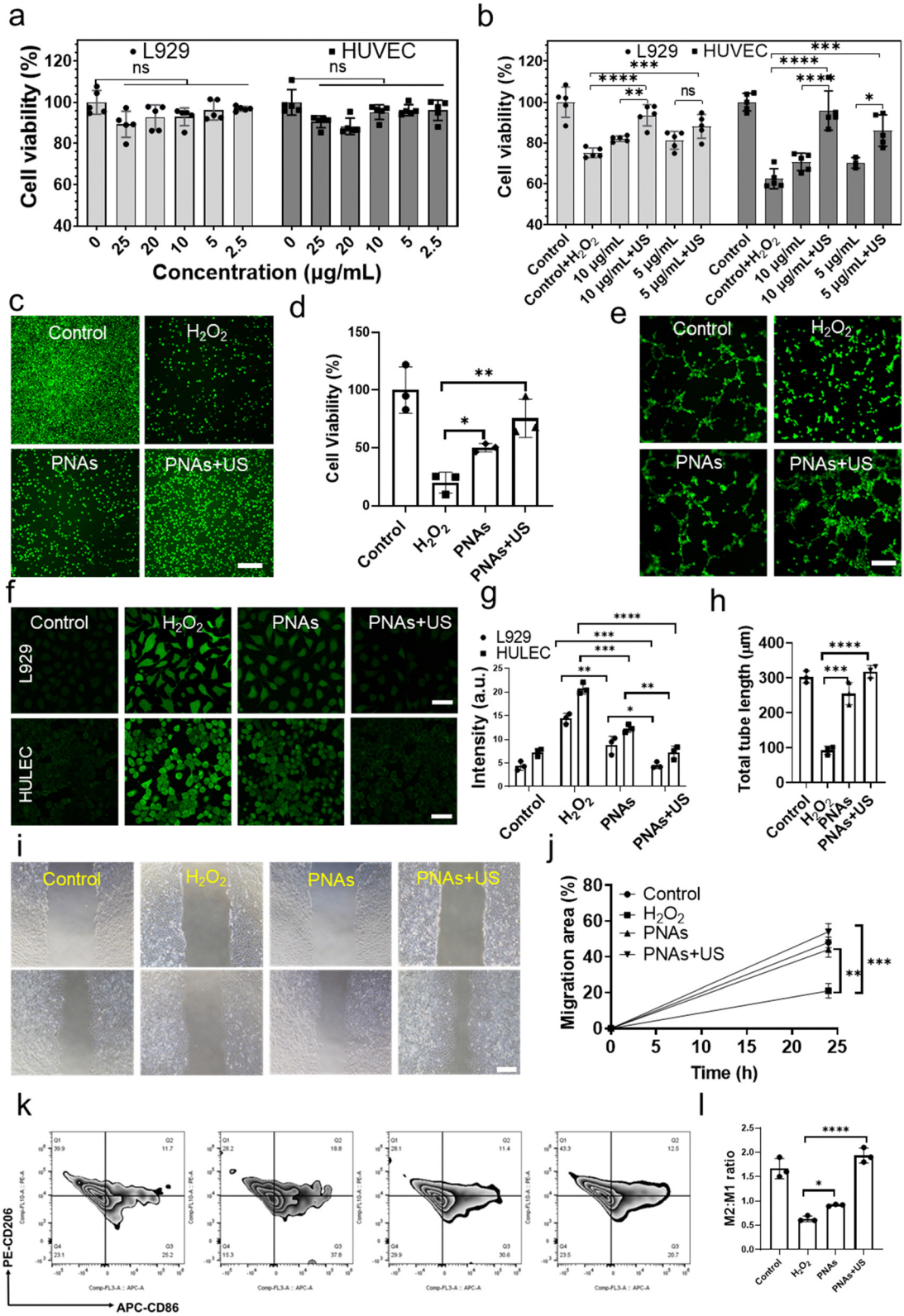

Fig. 4 ROS scavenging and macrophage polarization regulation by PNAs. (a) The biocompatibility of PNAs in L929 cells and HUVECs. (b) ROS scavenging and cell proliferation under different treatments. (c) and (d) Laser confocal microscope images and quantification of L929 cell proliferation under different treatments. (e) and (h) Laser confocal microscope images and quantification of tube formation of HUVECs under different treatments. (f) and (g) Laser confocal microscope images and quantification of the ROS scavenging ability of PNAs. (i) and (j) Laser confocal microscope images and quantification of HaCaT cell migration under different treatments. (k) and (l) Flow cytometry analysis and quantification of macrophage polarization regulation.

elimination. The effect of PNAs on L929 cell proliferation was further evaluated by staining live cells (Fig. 4c and d). The cell proliferation induced by PNAs and PNAs + US was significantly higher than that in the H_2O_2 group.

Next, we employed a fluorescence microscope to study the ROS scavenging performance of PNAs and PNAs under ultrasound radiation. To simulate the inflammatory microenvironment of diabetic wounds, we established a cell oxidative stress model induced by H_2O_2 as a control group. As shown in Fig. 4f and g, PNAs serve as potent regulators of intracellular ROS levels within L929 and HUVECs. These results demonstrate that although PNAs possess decent ROS scavenging capabilities in comparison to the H_2O_2 group, their ROS scavenging performance is most potent when applied with US. These observations correlated with the characterization that established the capability of PNAs to catalyze GSH production under US. Theoretically, under high cellular oxidative stress, PNAs under ultrasound radiation could efficiently catalyze the conversion of intracellular GSSG to GSH, hence enabling further ROS scavenging by utilizing GSH while catalyzing H_2O_2, thereby achieving an enhanced ROS scavenging effect. Next, we examined the influence of PNAs on ROS-induced HUVECs and HaCaT cells. ROS significantly inhibited HUVEC tube formation and HaCaT migration. We performed tube formation tests using a fluorescence microscope. The Matrigel tube formation assay, performed to assess angiogenic capacity, revealed a significantly greater tube length and branches assessed after 6 h in PNA + US-treated HUVECs than in PNA-treated HUVECs (Fig. 4e and h). Subsequently, we investigated the influence of PNAs and PNAs under ultrasound radiation on ROS-induced HaCaT cells. ROS significantly inhibited HaCaT cell migration, while PNA stimulation significantly increased cell migration, with the effect of PNAs under ultrasound radiation on cell migration being more pronounced, significantly surpassing both the H_2O_2 group and the control group (Fig. 4i and j). Macrophages play a key role in skin regeneration during the wound healing process. Quantitative analysis and ratio evaluation of $CD206^+$ (M2 macrophages) and $CD86^+$ (M1 macrophages) cells were conducted using flow cytometry (Fig. 4k and l). Compared to the other groups, the highest populations of M2 macrophages and the lowest populations of M1 macrophages were observed in the PNAs + US group, indicating a reduced proinflammatory cell capacity and anti-inflammatory cell enhancement. These results implied that the observed ROS scavenging effect in a series of *in vitro* assays can be attributed to the antioxidase functions of PNAs and their ability to generate GSH under US.

In vivo diabetic wound healing evaluation of PNAs

Benefiting from the antioxidative and anti-inflammatory properties of PNAs, which mimic CAT and POD enzymes and the generation of GSH under US, both PNAs and PNAs under ultrasound radiation promoted the proliferation of fibroblasts, the differentiation of endothelial cells, HaCaT cell migration, and accelerated healing of diabetic wounds. We applied a blend of PNAs with GelMA gel for wound healing therapy, as depicted in Fig. 5a. Images of wound healing at different time points following different treatment modalities, traces of wound closure, and corresponding quantitative wound healing analysis are provided in Fig. 5b and c.

In the GelMA + PNAs + US group, US therapy was administered only once at the wound site after the first day of dosing. On day 3, the wound area in the GelMA + PNAs + US group with a wound closure of 70% was noticeably smaller than that in the other groups. On day 5, the wound area in the GelMA + PNAs + US group had further decreased. On day 7, the wound closure area was 67% in the GelMA + PNAs group and 87% in the GelMA + PNAs + US group, while in the control and GelMA groups, the wound closure areas remained at 47% and 59%, respectively. On day 9, 95% of the wounds in the GelMA + PNAs + US treatment had closed, in contrast to the control and GelMA groups, which still exhibited obvious wound areas, and the GelMA + PNAs group, where wound closure was 76%. These results indicate that both PNAs and PNAs + US can accelerate the healing rate of diabetic wounds, with the effect being particularly pronounced for PNAs in the presence of US. As illustrated in Fig. 5d and e, histological examination of the healing wound was studied by both hematoxylin-eosin (H&E) and Masson's trichrome (MT) staining. As revealed by the H&E images, the GelMA + PNAs + US group presented a desirable capacity in diabetic wound healing by accelerating both epidermis and dermis formation. The quantitative analysis of epidermal thickness and collagen deposition on day 9 is shown in Fig. 5f and g. While evidence of epidermal regeneration was observed in all groups, the epidermis of the GelMA + PNAs + US faction was more natural and mature than that of the other groups and displayed an augmented collagen deposition level.

In fact, the green fluorescence signal was virtually undetectable in the GelMA + PNAs + US group. Such observations demonstrated that PNAs + US can effectively scavenge ROS, thereby alleviating oxidative stress (Fig. 6a and e). We assessed the oxygenation capability of PNAs on wounds through immunofluorescence staining of hypoxia-inducible factor 1-alpha (HIF-1α). The control and GelMA groups confirmed significant HIF-1α expression. Owing to the PNA nanozyme activity, the level of HIF-1α in the PNA group was obviously lower than that in the two other groups, indicating an enhanced O_2 supply (Fig. 6b and f). Fig. 6c and g illustrate a biological process exploration involved in wound healing, achieved *via* epidermal growth factor (EGF) immunofluorescence staining on day 6. EGF expression was examined in both the GelMA + PNAs and GelMA + PNAs + US groups, suggesting that the capacity to supply O_2 and scavenge ROS promotes EGF expression. GelMA + PNAs + US treatment was associated with the highest EGF expression, implying that O_2 generation and ROS scavenging are crucial for epidermal formation. Moreover, vascular endothelial growth factor (VEGF), widely considered a critical downstream marker of HIF, is suppressed under hypoxic conditions. The VEGF immunofluorescence staining and its quantitative analysis are shown in Fig. 6d and h, with the GelMA + PNAs + US group exhibiting a higher level, suggesting more blood vessel formation attributable to the hydrogel, O_2 delivery, and ROS scavenging.

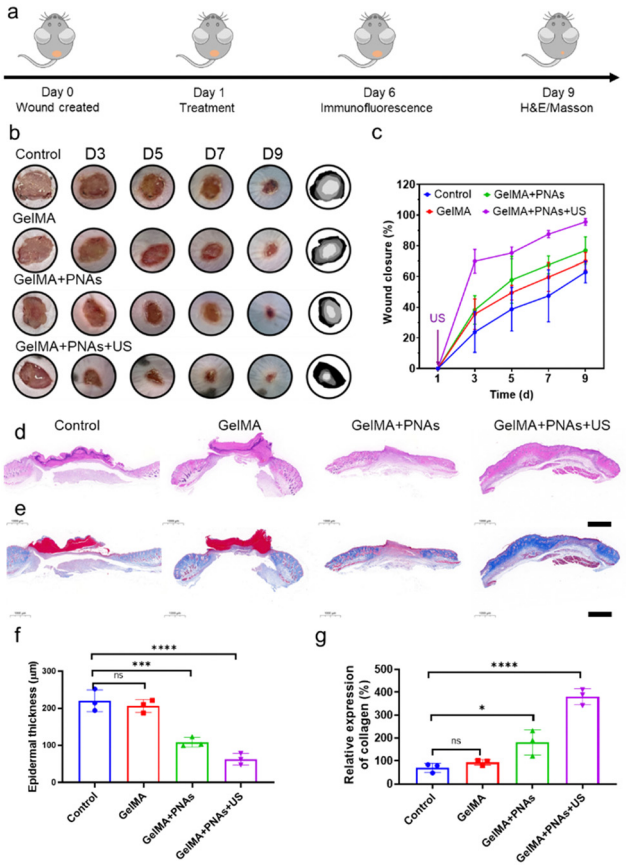

Fig. 5 Effects of the PNAs on enhancing diabetic wound healing in mice. (a) Schematic depiction of the sequence of animal experiments conducted to evaluate the therapeutic efficacy of PNAs. (b) Photographs of representative wounds from various treatments. (c) Quantitative investigation of the wound area. (d) HE and (e) Masson wound staining on day 9. Scale bars: 1000 μm. (f) and (g) Relative quantitative analysis on day 9 of collagen deposition and epidermis thickness. Data are presented as the mean ± s.d. (n = 3 independent mice).

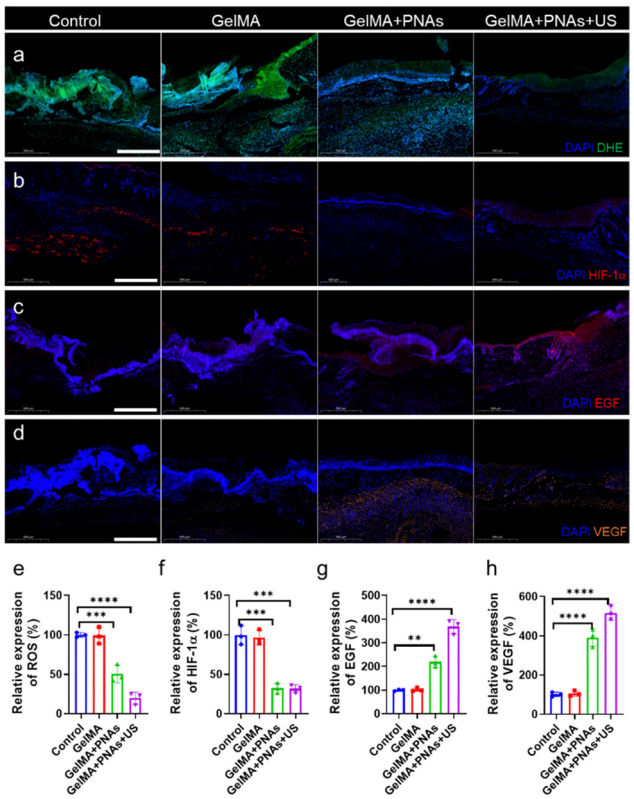

Fig. 6 Analysis of the processes and mechanisms of wound healing for various treatments. (a) ROS content, (b) HIF-1α expression, (c) EGF expression, and (d) VEGF expression at day 6 under various treatments. Scale bars: 500 μm. (e)–(h) Quantitative investigation of ROS, HIF-1α, EGF, and VEGF expression on day 9 in response to various treatments. Data are presented as the mean ± s.d. (n = 3 independent mice).

Angiogenesis, an important marker in diabetic wound healing, was evaluated through coimmunofluorescence staining of alpha-smooth muscle actin (α-SMA) and CD31 to assess neovascularization. As revealed in Fig. 7a and d, CD31 expression in the GelMA + PNAs + US group was significantly greater than that in the three other groups, indicating the superior provascularization capability of PNAs + US. Furthermore, immunofluorescent costaining of collagen and the fibroblast marker vimentin was used to assess collagen deposition in granulation tissue (Fig. 7b and e). The augmentation of matrix deposition and the oriented alignment of collagen fibers enhanced ECM formation. The control and GelMA groups exhibited minimal collagen content, while the GelMA + PNAs + US group displayed high levels of collagen deposition and orientational alignment, thereby signaling better collagen production favorable to wound healing. Additionally, CD206 and CD86 immunofluorescence costaining further validated the *in vivo* M2/M1 macrophage ratio (Fig. 7c and f). The GelMA + PNAs and GelMA + PNAs + US groups presented elevated M2 macrophage populations, leading to a higher M2/M1 macrophage ratio, demonstrating the satisfactory anti-inflammatory capacity of PNAs + US.

Operating as a keystone modulator in the inflammatory response, nuclear factor-κB (NF-κB) curtails the progression of tissue regeneration by instigating the expression of a cadre of pro-inflammatory cytokines, specifically TNF-α, IL-6, and IL-1β. Neutrophils, the primary effector cells in bacterial infections, persistently accumulate in diabetic wounds, consequently delaying the healing process. CXCL-1, an integral constituent of the CXC chemokine family, orchestrates both the migration and activation of neutrophils. The GelMA+PNAs + US group exhibited a significant downregulation of IL-1β, IL-6, TNF-α, and CXCL-1 compared with the other groups, denoting its superior efficacy in mitigating inflammation (Fig. S7, ESI†). In contrast, IL-4 and IL-10 emerge as cytokines favoring a regenerative milieu, contributing to the multifaceted processes of tissue repair, wound healing, axonal regeneration, and M2 macrophage polarization. Compared to the control and GelMA groups, the PNAs + US group exhibited the highest levels of IL-4 and IL-10, demonstrating an obvious regenerative impact. Posttreatment, a notable decrease in the proportions of peripheral blood leukocytes (WBCs), lymphocytes (Lymphs), and neutrophils (Grans) was observed in both the GelMA+PNAs and GelMA+PNAs + US groups compared to the control and

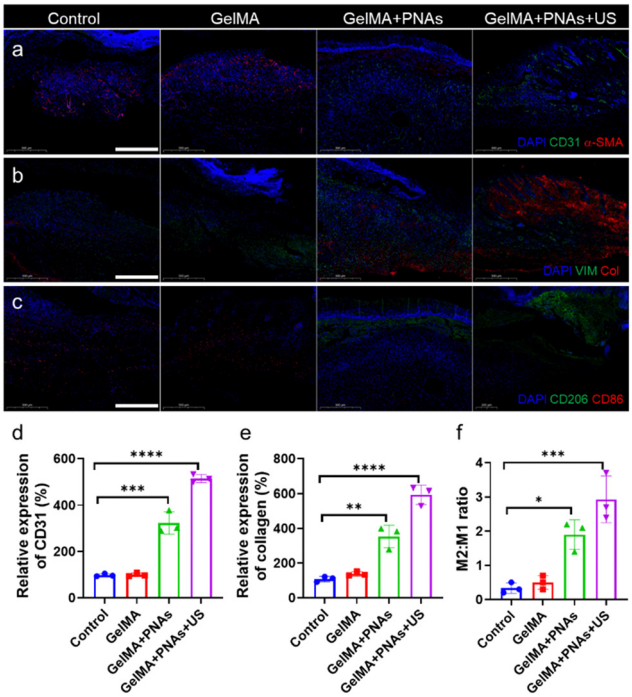

Fig. 7 Double immunofluorescence staining of (a) α-SMA (red) and CD 31 (green), (b) fibroblast marker vimentin (green) and collagen (red), (c) CD206 (green) and CD86 (red) in response to various treatments on day 6. Scale bars: 500 μm. (d)–(f) Quantitative investigation of CD31, collagen I deposition, and the M2 : M1 ratio at day 9 in response to various treatments. Data are presented as the mean ± s.d. (n = 3 independent mice).

GelMA groups. It can be inferred that the synergistic effects of ROS clearance, antioxidation, and anti-inflammation within the PNAs + US group significantly contribute to reducing wound inflammation.

Conclusions

In this study, we designed a nanozyme that emulates antioxidase activity and mimics the action of glutathione reductase under ultrasound. This nanozyme catalyzes the consumption of H_2O_2 and generates GSH, effectively scavenging ROS and combating inflammation, thus promoting the rapid healing of diabetic wounds. The multifunctional properties of PNA nanozymes originate from a synthesis strategy that employs a metal–organic coordination polymer hybridized *via* dynamic covalent bonds as a fabrication template. This approach facilitates control over the interparticle distances between platinum nanoparticles, prompting their high-density aggregation into compact nanoassemblies. The outer polymeric layer of PNAs serves to effectively protect the catalytic activity of platinum nanoparticles, enabling them to exhibit their inherent catalytic properties and mimic the antioxidative enzyme activities of CAT and POD. Additionally, the nanoconfinement ability of the outer polymeric material imposes diffusion limitations on the platinum nanoparticles, altering their interparticle distances. This attribute endows the PNAs with a plasmonic resonance effect under ultrasound, promoting electron polarization, which enables the transfer of H from NADPH to the substrate GSSG, resulting in GSH production. A series of enzymatic kinetic studies have confirmed the ability of PNAs to mimic CAT and POD, catalyzing H_2O_2 to produce O_2 and H_2O, and have also validated that PNAs, under ultrasound, can simulate GR to catalyze the generation of GSH. The data obtained in our study revealed that PNAs under ultrasound can restore the proliferative capacity of cells in high oxidative stress environments, effectively decrease the ROS level, enhance cell migration abilities, and promote M2 anti-inflammatory macrophage polarization. Incorporating PNAs into GelMA hydrogel has demonstrated significant efficacy in enhancing wound healing *in vivo* for chronic diabetic wounds. We are convinced that this multifunctional PNA nanoenzyme-based approach offers a superior strategy for improving the healing process of chronic wounds.

Author contributions

X. Ji, F. Zhang, S. Koo, W. Tao, and T. Luan designed and supervised the project. X. Ji, F. Zhang, and Y. Kang designed the experimental strategies. F. Zhang, Y. Kang and L. Feng performed the experiments and analyzed the data. X. Ji and F. Zhang wrote the manuscript. S. Koo, W. Tao, W. Chen, and N. Kong revised the manuscript.

Conflicts of interest

There are no conflicts to declare.

Acknowledgements

This study was financially supported by a grant from the National Natural Science Foundation of China (Grant No. 32071322, to X. J.; 22127810, to T. L.), the National Natural Science Funds for Excellent Young Scholar (Grant No. 32122044; to X. J.), Guangdong Basic and Applied Basic Research Foundation (Grant No. 2020A1515110091; to F. Z.), the Technology & Innovation Commission of Shenzhen Municipality (Grant No. JCYJ20210324113004010; to X. J.), and National Research Foundation of Korea (Grant No. 2022R1C1C2007637; to S. K.).

Notes and references

1 J. Ouyang, X. Ji, X. Zhang, C. Feng, Z. Tang, N. Kong, A. Xie, J. Wang, X. Sui, L. Deng, Y. Liu, J. S. Kim, Y. Cao and W. Tao, *Proc. Natl. Acad. Sci. U. S. A.*, 2020, **117**, 28667–28677.
2 International Diabetes Federation, *IDF Diabetes Atlas (IDF)*, 2022.
3 I. Visan, *Nat. Immunol.*, 2019, **20**, 1089.
4 W. Zhang, S. Xia, T. Weng, M. Yang, J. Shao, M. Zhang, J. Wang, P. Xu, J. Wei, R. Jin, M. Yu, Z. Zhang, C. Han and X. Wang, *Mater. Today Bio.*, 2022, **16**, 100395.
5 Q. Wang, G. Zhu, X. Cao, J. Dong, F. Song and Y. Niu, *J. Diabetes Res.*, 2017, **2017**, 1428537.

6 A. E. Louiselle, S. M. Niemiec, C. Zgheib and K. W. Liechty, *Transl. Res.*, 2021, **236**, 109–116.
7 H. Zhao, J. Huang, Y. Li, X. Lv, H. Zhou, H. Wang, Y. Xu, C. Wang, J. Wang and Z. Liu, *Biomaterials*, 2020, **258**, 120286.
8 Y. Zhu, Y. Wang, Y. Jia, J. Xu and Y. Chai, *Wound Repair. Regener.*, 2019, **27**, 324–334.
9 R. Lobmann, A. Ambrosch, G. Schultz, K. Waldmann, S. Schiweck and H. Lehnert, *Diabetologia*, 2002, **45**, 1011–1016.
10 M. Chang and T. T. Nguyen, *Acc. Chem. Res.*, 2021, **54**, 1080–1093.
11 L. Jiang, X. Yang, Y. Zhang, D. He, Y. Gao, K. Lu, Y. Hao, Y. Gao, D. Lu, X. Jin and C. Li, *Biomater. Adv.*, 2023, **144**, 213226.
12 A. U. R. Khan, K. Huang, M. S. Khalaji, F. Yu, X. Xie, T. Zhu, Y. Morsi, Z. Jinzhong and X. Mo, *Bioact. Mater.*, 2021, **6**, 2783–2800.
13 P. Mishra, J. Lee, D. Kumar, R. O. Louro, N. Costa, D. Pathania, S. Kumar, J. Lee and L. Singh, *Adv. Funct. Mater.*, 2021, **32**, 2108650.
14 D. Jiang, D. Ni, Z. T. Rosenkrans, P. Huang, X. Yan and W. Cai, *Chem. Soc. Rev.*, 2019, **48**, 3683–3704.
15 J. Sheng, Y. Wu, H. Ding, K. Feng, Y. Shen, Y. Zhang and N. Gu, *Adv. Mater.*, 2023, DOI: **10.1002/adma.202211210**.
16 Z. Wang, R. Zhang, X. Yan and K. Fan, *Mater. Today*, 2020, **41**, 81–119.
17 S. Dong, Y. Dong, B. Liu, J. Liu, S. Liu, Z. Zhao, W. Li, B. Tian, R. Zhao, F. He, S. Gai, Y. Xie, P. Yang and Y. Zhao, *Adv. Mater.*, 2022, **34**, 2107054.
18 R. Zhang, B. Xue, Y. Tao, H. Zhao, Z. Zhang, X. Wang, X. Zhou, B. Jiang, Z. Yang, X. Yan and K. Fan, *Adv. Mater.*, 2022, **34**, 2205324.
19 K. Dehvari, S. H. Chiu, J. S. Lin, W. M. Girma, Y. C. Ling and J. Y. Chang, *Acta Biomater.*, 2020, **114**, 343–357.
20 L. Zhang, C. Zhang, Z.-N. Zhuang, C.-X. Li, P. Pan, C. Zhang and X.-Z. Zhang, *Sci. China: Chem.*, 2021, **64**, 616–628.
21 L. Wang, B. Zhu, Y. Deng, T. Li, Q. Tian, Z. Yuan, L. Ma, C. Cheng, Q. Guo and L. Qiu, *Adv. Funct. Mater.*, 2021, **31**, 2101804.
22 A. K. Horst, K. G. Kumashie, K. Neumann, L. Diehl and G. Tiegs, *Cell Mol. Immunol.*, 2021, **18**, 92–111.
23 J. Muri and M. Kopf, *Nat. Rev. Immun.*, 2021, **21**, 363–381.
24 A. V. Ferreira, V. Koeken, V. Matzaraki, S. Kostidis, J. C. Alarcon-Barrera, L. C. J. de Bree, S. Moorlag, V. P. Mourits, B. Novakovic, M. A. Giera, M. G. Netea and J. Dominguez-Andres, *Cells*, 2021, **10**, 971.
25 T. Liu, L. Sun, Y. Zhang, Y. Wang and J. Zheng, *J. Biochem. Mol. Toxicol.*, 2022, **36**, e22942.
26 F. Ursini and M. Maiorino, *Free Radical Biol. Med.*, 2020, **152**, 175–185.
27 L. Bai, X. Wang, Q. Chen, Y. Ye, H. Zheng, J. Guo, Y. Yin and C. Gao, *Angew. Chem., Int. Ed.*, 2016, **55**, 15656–15661.
28 X. Jiao, C. Batchelor-McAuley, C. Lin, E. Kätelhön, E. E. L. Tanner, N. P. Young and R. G. Compton, *ACS Catal.*, 2018, **8**, 6192–6202.
29 C. L. Yang, L. N. Wang, P. Yin, J. Liu, M. X. Chen, Q. Q. Yan, Z. S. Wang, S. L. Xu, S. Q. Chu, C. Cui, H. Ju, J. Zhu, Y. Lin, J. Shui and H. W. Liang, *Science*, 2021, **374**, 459–464.
30 Y. Negrin-Montecelo, X. T. Kong, L. V. Besteiro, E. Carbo-Argibay, Z. M. Wang, M. Perez-Lorenzo, A. O. Govorov, M. Comesana-Hermo and M. A. Correa-Duarte, *ACS Appl. Mater. Interfaces*, 2022, **14**, 35734–35744.
31 W. Feng, X. Han, H. Hu, M. Chang, L. Ding, H. Xiang, Y. Chen and Y. Li, *Nat. Commun.*, 2021, **12**, 2203.
32 D. Wei, X. Zhang, B. Chen and K. Zeng, *Anal. Chim. Acta*, 2020, **1126**, 106–113.
33 Y. Zhu, J. Wu, K. Wang, H. Xu, M. Qu, Z. Gao, L. Guo and J. Xie, *Talanta*, 2021, **224**, 121852.
34 C. B. Liu, Z. Li and Z. X. Zhang, *J. Biol. Phys.*, 2009, **35**, 175–183.
35 M. A. El-Sayed, *Acc. Chem. Res.*, 2001, **34**, 257–264.
36 D. S. Berkholz, H. R. Faber, S. N. Savvides and P. A. Karplus, *J. Mol. Biol.*, 2008, **382**, 371–384.
37 I. Willner, N. Lapidot, A. Riklin, R. Kasher, E. Zahavy and E. Katz, *J. Am. Chem. Soc.*, 1994, **116**, 1428–1441.
38 U. F. Fritze and M. V. Delius, *Chem. Commun.*, 2016, **52**, 6363–6366.